Influence of low-pulsed frequency on arc profile and weld formation characteristics in double-pulsed VPTIG welding of aluminium alloys

Wang Yipeng[1,2], Cong Baoqiang[*1], Qi Bojin[*1], Chen Xin[2], Yin Yuhuan[3], Lin Sanbao[4]

[1]School of Mechanical Engineering and Automation, Beihang University, Beijing 100191, China

[2]Welding Engineering and Laser Processing Centre, Cranfield University, Cranfield, United Kingdom

[3] Shanghai Aerospace Equipments Manufacturer Co., Ltd., Shanghai 200245, China

[4] Key Lab of Advanced Welding and Joining, Harbin Institute of Technology, Harbin 150001, China

*Corresponding authors, email: congbq@buaa.edu.cn, qbj@buaa.edu.cn;   Tel/Fax: +86-(0)10-82338722

Abstract: AA2219 aluminium alloy plates were processed by double pulsed variable polarity tungsten inert gas (DP-VPTIG) welding, and the influence of low-pulsed frequency on arc profile, weld appearance and penetration characteristics were investigated. An image processing algorithm was proposed for arc edge extraction and arc feature sizes acquisition. The arc energy equations in low-frequency pulse peak stage (t_p) and base stage (t_b) were established based on the electrical parameters. The arc profile periodically expanded in t_p and shrunk in t_b, resulted from the difference in arc energy of the two stages. The pulsation effects in arc profile, weld appearance and penetration, caused by the pulsed arc were observed to exhibit a decreasing trend with the increase of low-pulsed frequency (f_L). The pulsation effects were obvious when f_L was 0.5 Hz, then became weak and tended to disappear as f_L increased above 3 Hz. The empirical correlations between f_L and the pulsation effects of arc profile, weld appearance and penetration were respectively developed. It is recommended to use f_L in the range of 1–2 Hz to properly exert the low-frequency pulsation effect. The results provide a valuable basis for controlling and optimizing the DP-VPTIG process in the high efficiency welding of aluminum alloys.

Keywords: welding arc, double pulses, weld formation, tungsten inert gas welding, aluminium alloy

1. Introduction

Aluminium alloys have been extensively applied in the fields of aviation, aerospace and automobile industries owing to their excellent fracture toughness, corrosion resistance and high specific strength [1]. Due to the advantages of cathode cleaning effect on removal of the surface oxide film and high operational flexibility, variable polarity tungsten inert gas (VPTIG) welding process is widely adopted in the welding of aluminium alloys [2]. However, the penetration depth of VPTIG unconstrained welding arc is relatively low caused by the limitation of current-carrying capacity of the non-consumable electrode, which leads to low production efficiency and greatly limits its further application [3]. With the purpose to promote the welding efficiency and satisfy the growing demand for the high-quality TIG welding, investigators have done a large amount of research work, involving the use of mixed shielding gases [4], the application of assistant measures (external magnetic field, ultrasound) [5], the variants of conventional TIG process (A-TIG – activated TIG, K-TIG – keyhole TIG, CF-TIG – cathode focused TIG, multiple-electrodes TIG) [6], the introduction of pulsed arc (high-frequency pulse, low-frequency pulse) [7] , etc.

Current pulsing achieved by modulating the current waveform of the power source has been considered to be one of the most flexible and effective method to improve the arc properties and weld quality. Yang et al. [8] indicated that the welding arc was distinctly constricted and the arc force was largely enhanced by

high-frequency pulsed welding (20 kHz, 40 kHz) in comparison to the conventional TIG welding. Fang et al. [9] experimentally found that the high-frequency pulse (around 40 kHz) was beneficial to increase the weld penetration and expand the current window in K-TIG welding of Q345 steel plates. Yang et al. [10] demonstrated that compared with conventional TIG welding, the refinement of grain size in weld zone and the improvement of tensile properties were realized by high-frequency pulsed welding with 20% duty cycle. The low-frequency pulsed current (1–1.5 Hz) was proved to effectively stabilize the high efficiency welding of 304 stainless steel with a wider current window [11]. The grain structure was refined contributed by the oscillating effect of the arc pressure in 2 Hz low-frequency pulsed VP-TIG welding [12].

To further improve the welding applicability of VPTIG to aluminium alloy plates, the variable polarity square wave current was simultaneously modulated into high-frequency (20–80 kHz) and low-frequency (0.5–10 Hz) pulses, referred as DP-VPTIG. The high-frequency pulse was used to enhance the arc penetrating ability, and the low-frequency pulse was used to flexibly adjust the balance of arc heat and force effects to stabilize the weld pool. Stable keyhole mode high penetration welding of 7 mm thick AA2219 aluminium alloy plate was successfully realized by DP-VPTIG process through properly adjusting the pulse current parameters [13]. Previous work has preliminarily revealed the dynamic evolution processes of the arc profile and weld pool morphology throughout a complete low-frequency pulse period in DP-VPTIG process [12, 14]. It has been found that low-pulsed frequency was an essential factor for the process stability and weld quality. As welding arc is the heat and force source of the welding process, it is necessary to deeply investigate the arc profile and corresponding weld formation characteristics under the effect of low-pulsed frequency, and explore its potential advantages in weld formation and quality control. In this study, the influence of low-pulsed frequency on arc profile and weld formation characteristics, reflected by weld appearance and weld penetration, in DP-VPTIG welding of AA2219 aluminium alloy plates were investigated.

2. Methodology

2.1. Experimental set-up

The experimental system for the observation of welding arc is schematically displayed in Fig. 1. This system mainly consisted of a self-developed DP-VPTIG welding power source, a screw motion system, a welding torch and its water cooling system, the shielding gas and an image acquisition system. The acquisition system was primarily composed of a CMOS-based high-speed camera (MS 75K) and a real-time control and recording system on a computer. A close-focusing macro lens (Navitar ZOOM 7000) with a neutral-density filter was installed on the camera. The camera was fixed by the side of the motion system, and its lens focused on the area around the electrode tip. During welding, the welding torch was kept stationary, while the work-piece moved with the motion system.
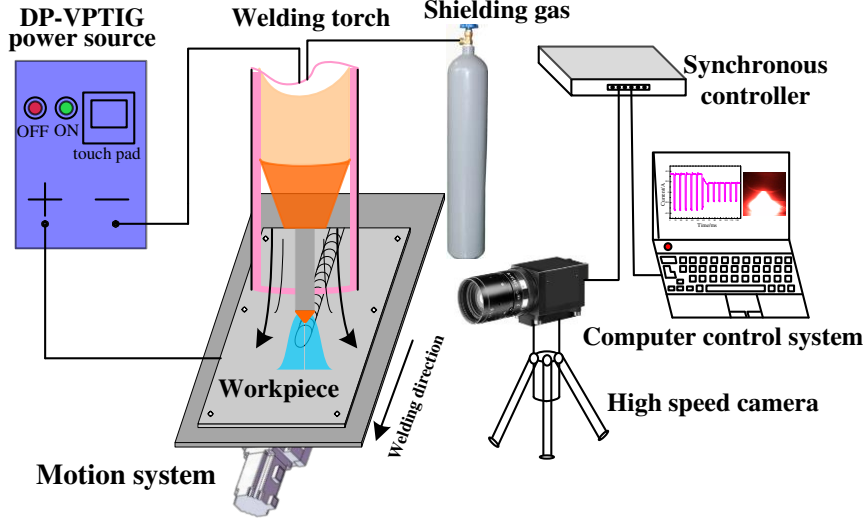
Fig.1 Schematic diagram of the welding system

The schematic diagram of DP-VPTIG current waveform is illustrated in Fig. 2. The variable polarity square wave was modulated into low-frequency pulses (0.5–10 Hz), and the high-frequency pulses (20– 80 kHz) were superposed onto the positive polarity stage. In the figure, T_v is the period of variable polarity square wave, t_{vp} is the duration of positive stage, t_{vn} is the duration of negative stage, T_L is the period of low-frequency pulse, t_p is the duration of low-frequency pulse peak stage, t_b is the duration of low-frequency pulse base stage, I_{pp} is the positive current during t_p, I_{pn} is the negative current during t_p, I_{bp} is the positive current during t_b, I_{bn} is the negative current during t_b, I_{HP} is the amplitude of high-frequency pulse. Limited by the design of the main circuit topology, I_{pp} and I_{pn}, I_{bp} and I_{bn} couldn't be set separately, namely $I_{pp}= I_{pn}$ and $I_{bp}= I_{bn}$. To simplify the description in the following discussion, I_p and I_b were used to represent the low-frequency pulse peak current (I_{pp}/I_{pn}) and base current (I_{bp}/I_{bn}), respectively.
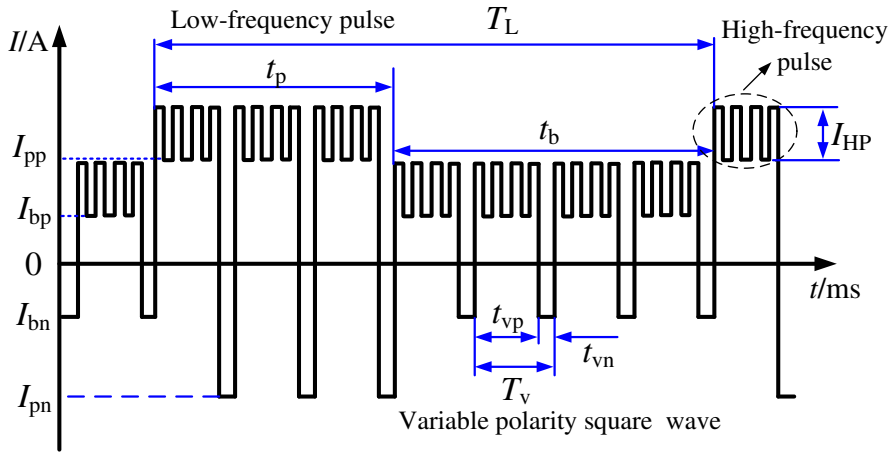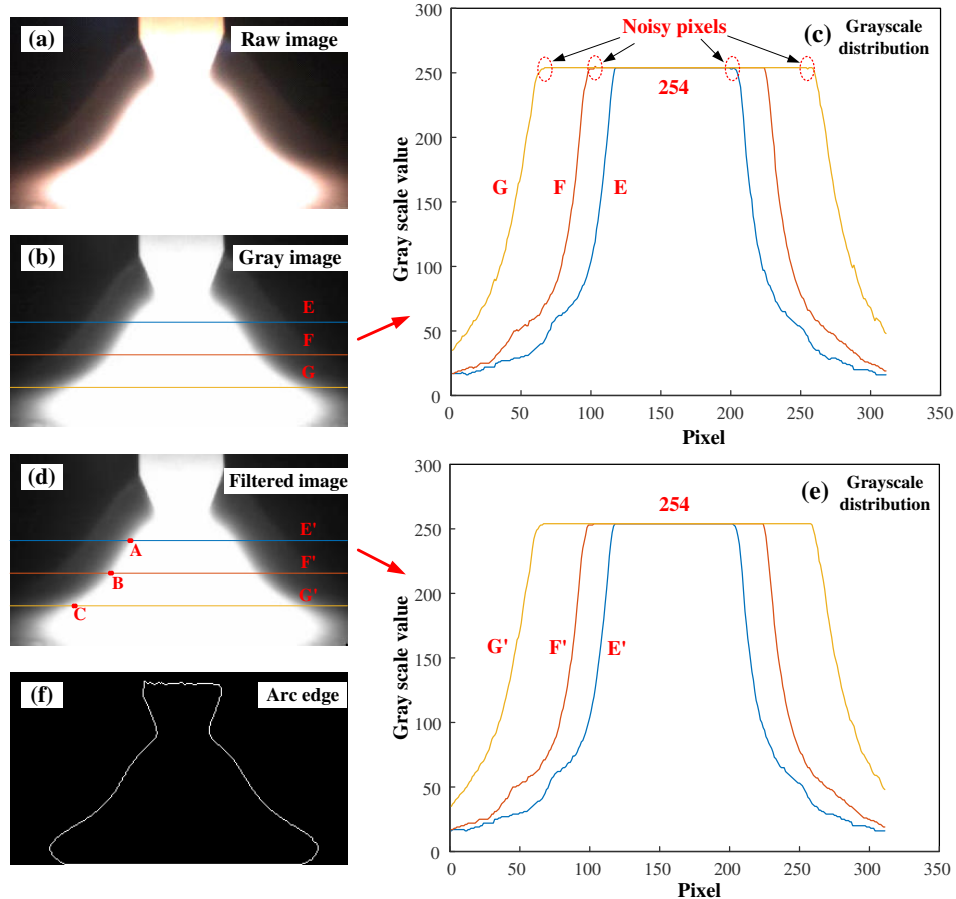

Fig.2 Schematic diagram of DP-VPTIG current waveform

2.2. Arc edge extraction

To investigate the arc profile characteristics, it is necessary to first identify and extract the clear arc edge, so as to obtain the appropriate feature sizes for the representation of the arc profile. The arc edge extraction algorithm mainly included the following steps.

3

Fig.3 Image processing procedure for arc edge extraction.

(1) *Grayscale transformation*. The arc raw image (311*176 pixels) displaying in Fig.3a was converted into a 256-level grayscale image, as shown in Fig.3b. In the grayscale image, the light intensity was classified into 256 levels. A higher grayscale value indicated a higher light intensity.

(2) *Image de-noising*. The grayscale value distribution of the specific lines E, F and G is shown in Fig.3c. It can be found that there were some noisy pixels with grayscale values obviously different from those of the adjacent pixels, which may lead to the misrecognition of the arc edge. To supress these noisy pixels, the median filter with a window size of 3×3 was employed. The de-noised image and its corresponding grayscale value distribution are illustrated in Fig.3d and Fig.3e, respectively. The noisy pixels were effectively reduced without blurring the edge of the arc.

(3) *Arc edge extraction*. As displayed in Fig.3e, the image had an obvious contrast between the arc area and the background. The grayscale value rose monotonically as the pixel approached to the arc edge. In the arc central region, the grayscale value became nearly saturated (254), corresponding to the highest light intensity. Here, 95% of the saturated grayscale value (242) was selected as the threshold value to distinguish the arc edge from the background. The grayscale values were converted into binary values of 1 (higher than threshold value) or 0

4

(lower than threshold value). The interior pixels were then removed to leave an outline of the arc shape. The edge extracted image is shown in Fig.3f, in which continuous and clear arc edge was successfully obtained.

2.3. Arc feature sizes acquisition and calibration

As shown in Fig.4, the arc projected size (D_B), arc electrode end size (D_E) and arc length (L) were used to reflect the feature sizes of welding arc profile [15]. From the edge extracted image, it is obvious that the arc started to expand from the electrode end, and its radial dimension increased continuously until arriving at the work-piece end. Namely, D_E was exactly the minimum distance between the two edges of the arc along X-axis, while D_B was the maximum one. The arc length L was the distance between the above two lines along Y-axis. Based on this point, a calculation and calibration algorithm to automatically acquire the dimensions of D_E, D_B and L was proposed by the following steps.
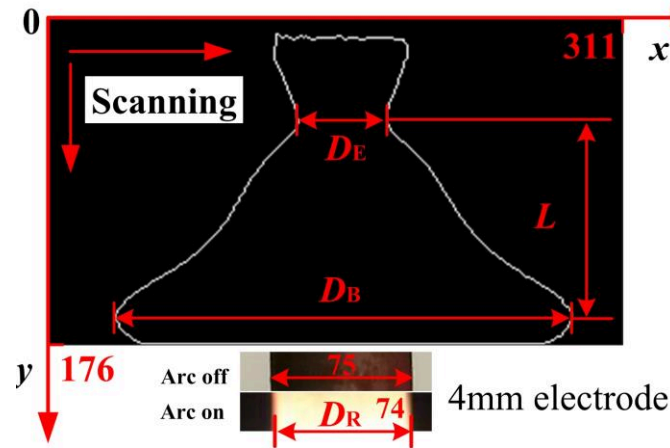

Fig.4 Arc feature sizes acquisition and calibration

(1) *Edge detection*. The grayscale values of each pixel horizontally along X-axis (X: 0–311, Y=0) were point-by-point scanned. The coordinate values were recognized and recorded when the grayscale value was 1, where the arc edge points in this X-axis line were located at. This step were repeated layer-by-layer along Y-axis (Y: 0–176) until all the arc edge points were detected.

(2) *Dimensions acquisition*. The distances between two arc edge points in each horizontal line were calculated. All the distances were then compared with each other, and D_E, D_B as well as L in pixels ($D_{E\text{-pixel}}$, $D_{B\text{-pixel}}$ and L_{pixel}) were acquired by the above mentioned idea.

(3) *Calibration*. To calibrate the three parameters from pixels to actual dimensions, the tungsten electrode with diameter of 4 mm ($D_{R\text{-pixel}}$ calculated in pixels) was selected as the reference dimension. As shown in the figure, there was a slight difference in electrode boundary when the arc was burning. The error in the measured value of the electrode diameter between arc burning and arc stop states was around 1%, which was considered acceptable. The calibration expressions were given by Equations 1–3.

$$D_E = K \cdot D_{E\text{-pixel}} \tag{1}$$

$$D_B = K \cdot D_{B\text{-pixel}} \tag{2}$$

$$L = K \cdot L_{\text{pixel}} \tag{3}$$

where $K = 4/ D_{\text{R-pixel}}$.

2.4. Process parameters

Bead-on-plate welding trials were carried out on 7 mm thick AA2219 aluminium alloy plates. To remove the impurities such as grease, oxide film and stains on the surface of the plates, the work-pieces were sequentially washed with alkaline water (NaOH 10% and H_2O 90%) and acid water (HNO_3 15% and H_2O 85%, all in volume fraction), and then cleaned with industrial alcohol and dried in air prior to welding. The shielding gas used was pure argon with a flow rate of 15L·min^{-1}. The electrode adopted was a cerium-tungsten with a diameter of 4 mm, and the cone angle of its front tip was 30 degrees. The welding speed was 170mm·min^{-1}. Six low-pulsed frequencies were used for the observation of arc profile, and the low-frequency pulse parameters are listed in Table 1. Other current parameters were T_v = 10 ms, $t_{\text{vp}}:t_{\text{vn}}$ = 8:2, I_{HP}=80 A, pulse frequency f_{HP}=20 kHz, duty cycle δ_{HP}=50%. The sampling frequency of the high-speed camera was 2000 frames per second, and the exposure time was 100 microseconds. The lens aperture of the camera was 5.6. As experimentally observed by Wang et al. [12], the arc profile gradually became stable when the current was switched from t_{vn} to t_{vp} throughout the variable polarity period. To ensure the consistency of the results, the arc images were all captured from t_{vp} at the same transient when they became stable.

Table 1. The welding parameters

Test No.	f_L/Hz	I_p/A	I_b/A	δ/%
1	0.5	240	100	50
2	1	240	100	50
3	2	240	100	50
4	3	240	100	50
5	5	240	100	50
6	10	240	100	50

3. Results and discussion

3.1 Arc profile variation between t_p and t_b

The arc images in t_p and t_b at low-pulsed frequency 0.5 Hz are displayed in Fig.5. Table 2 lists the sizes of arc projected size D_B, arc electrode end size D_E and arc length L of the corresponding arc images. In t_p, the arc profile was largely expanded due to the high current value. D_B, D_E and L were 17.0 mm, 3.3 mm and 6.3 mm, respectively. As welding current switched to t_b, the arc profile shrunk sharply because of the significant reduction in current value. The consequential sizes of D_B, D_E, and L reduced to 9.9 mm, 2.4 mm and 6.1 mm, respectively. The size of D_B, which directly acted on the surface of weld pool, changed most obviously (7.1 mm), while the changes of D_E and L were relatively small (0.9 mm and 0.2 mm) due to the restriction of the tungsten electrode tip.
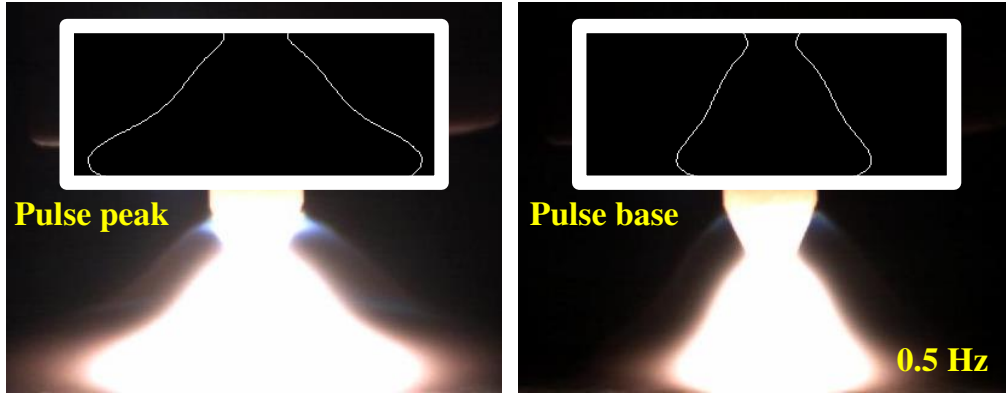
Fig.5 Arc images in t_p and t_b (f_L=0.5 Hz)

Table 2 Sizes of D_B, D_E and L in t_p and t_b (f_L=0.5 Hz)

Size\Stage	D_B/mm	D_E/mm	L/mm
t_p	17.0	3.3	6.3
t_b	9.9	2.4	6.1

It is known that the arc profile is a reflection of arc light energy, which is converted from the electric energy provided by the welding power source. Therefore, the variation in arc profile between t_p and t_b can be explained by the electrical characteristics of DP-VPTIG process. The current waveform with pulse frequency 0.5 Hz is shown in Fig.6. It can be observed that there were plenty of variable polarity square waves in both t_p and t_b. The high-frequency pulses were superimposed onto the positive stage in each variable polarity period. Due to the difference in amplitude value between t_p and t_b, the energy pulsation would occur when the current switched between the two stages. The arc light energy generated in t_p and t_b can be expressed by Equations 4 and 5, respectively.
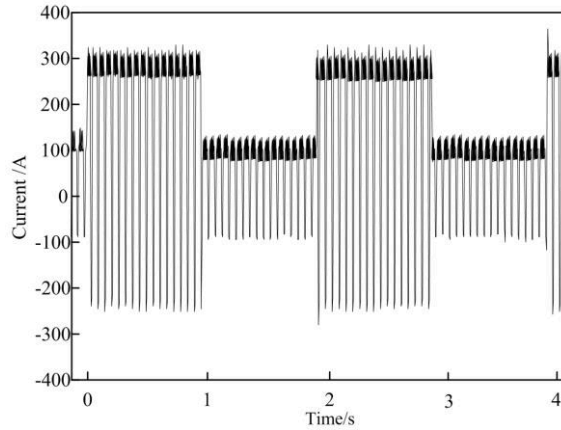

Fig.6 Current waveform of DP-VPTIG (f_L = 0.5 Hz)

$$
\begin{aligned}
Q_\mathrm{p} &= \eta_\mathrm{ARC} \cdot \int_0^{t_\mathrm{p}} u_\mathrm{t} i_\mathrm{t}\,\mathrm{d}t \\
&= \eta_\mathrm{ARC} \cdot \frac{f_\mathrm{v}}{f_\mathrm{L}} \cdot \delta \cdot \left[\int_0^{t_\mathrm{vp}} u_\mathrm{t} i_\mathrm{t}\,\mathrm{d}t + \int_\mathrm{vp}^{t_\mathrm{vn}} u_\mathrm{t} i_\mathrm{t}\,\mathrm{d}t \right] \\
&= \eta_\mathrm{ARC} \cdot \frac{f_\mathrm{v}}{f_\mathrm{L}} \cdot \delta \cdot \left[\left(I_\mathrm{pp} + I_\mathrm{HP\text{-}avg} \right) U_\mathrm{pp} + I_\mathrm{pn} U_\mathrm{pn} \right]
\end{aligned} \tag{4}
$$

$$Q_b = \eta_{ARC} \cdot \int_{t_p}^{t_b} u_t i_t \mathrm{d}t$$

$$= \eta_{ARC} \cdot \frac{f_v}{f_L} \cdot (1-\delta) \cdot \left[\int_0^{t_{vp}} u_t i_t \mathrm{d}t + \int_{t_{vp}}^{t_{vn}} u_t i_t \mathrm{d}t \right] \tag{5}$$

$$= \eta_{ARC} \cdot \frac{f_v}{f_L} \cdot (1-\delta) \cdot \left[\left(I_{bp} + I_{HP\text{-avg}} \right) U_{bp} + I_{bn} U_{bn} \right]$$

Where Q_p is the light energy in t_p, Q_b is the light energy in t_b, η_{ARC} is the conversion rate from electric energy to light energy, u_t is the transient voltage, i_t is the transient current, $I_{HP\text{-avg}} = I_{HP} \times \delta_{HP}$ is the average value of high-frequency current, U_{pp} is the positive voltage in t_p, U_{pn} is the negative voltage in t_p, U_{bp} is the positive voltage in t_b, U_{bn} is the negative voltage in t_b.

According to Equations 4 and 5, the arc light energy generated in t_p (Q_p) and t_b (Q_b) are determined by the electrical parameters of low-frequency pulse, high-frequency pulse and variable polarity square wave. In the case where current parameters of high-frequency pulse and variable polarity square wave remain constant, Q_p and Q_b are primarily affected by low-frequency pulse parameters. In the experimental condition, the amplitude value of I_p (240 A) is much higher than that of I_b (100 A), which means that the arc light energy in t_p is more than two times higher than that in t_b. Therefore, the arc profile variation between t_p and t_b are principally resulted from the large difference in arc light energy.
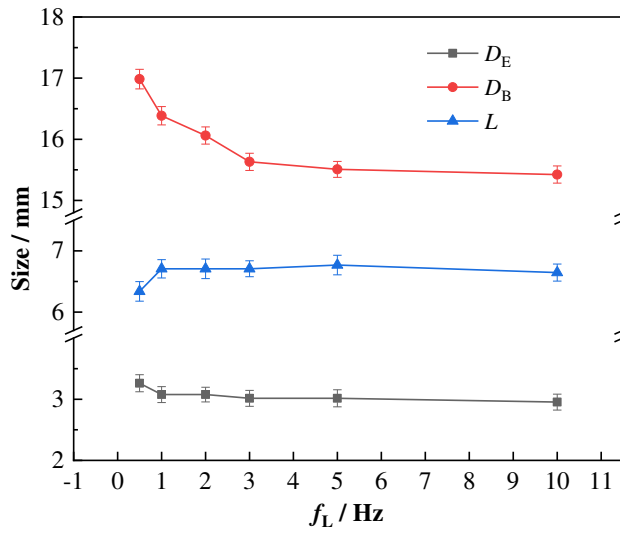
3.2. Effects of low-pulsed frequency on arc profile

Arc profile in t_p

The arc images and their corresponding feature sizes in low-frequency pulse peak stage at different f_L are shown in Fig.7a and Fig.7b, respectively. It can be seen that the size of D_B varied most significantly with f_L compared to those of D_E and L. D_B decreased monotonously with increasing f_L. When f_L changed from 0.5 to 3 Hz, the drop rate of D_B was relatively high, with its size falling down rapidly from 17.0 mm to 16.1 mm. As f_L further increased to the level higher than 3 Hz, the drop rate of D_B gradually became smaller, and its size slowly stabilized at around 15.5 mm. The arc electrode end size D_E presented a similar variation trend to that of D_B, but due to the restriction of the tungsten electrode, its changes with f_L were much smaller. D_E dropped from 3.3 mm to 3.0 mm as f_L varied from 0.5 Hz to 3 Hz. Then it decreased slowly to about 2.9 mm at 10 Hz. The arc length L showed an increasing trend with f_L. When f_L varied from 0.5 to 1 Hz, the size of L increased from 6.3 mm to 6.7 mm with a relatively high rising rate. It then fluctuated slightly between 6.6 mm and 6.7 mm as f_L further increased. In t_p, the arc profile shrunk, representing that D_B and D_E decreased and L increased, as f_L increased.
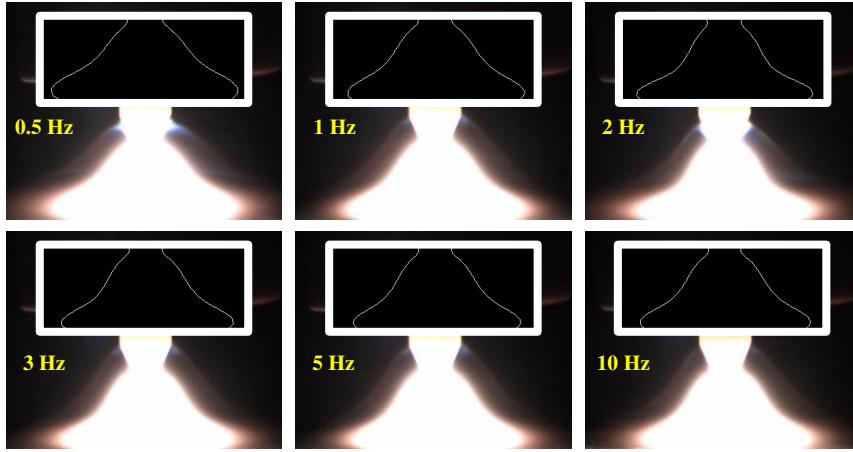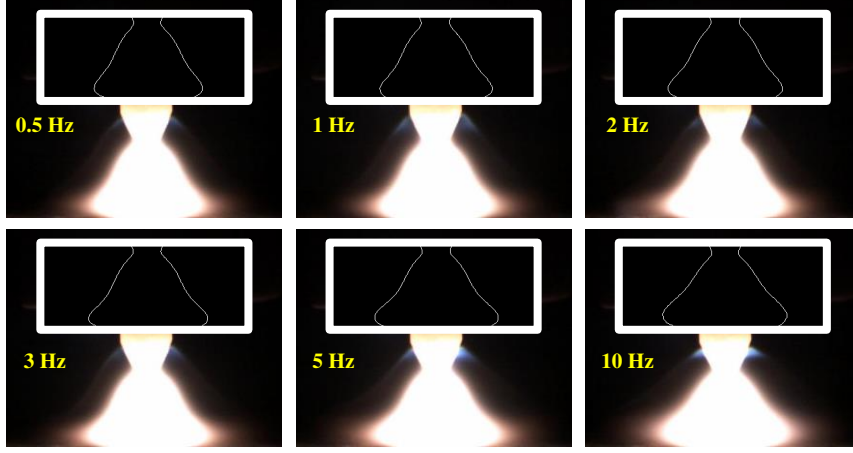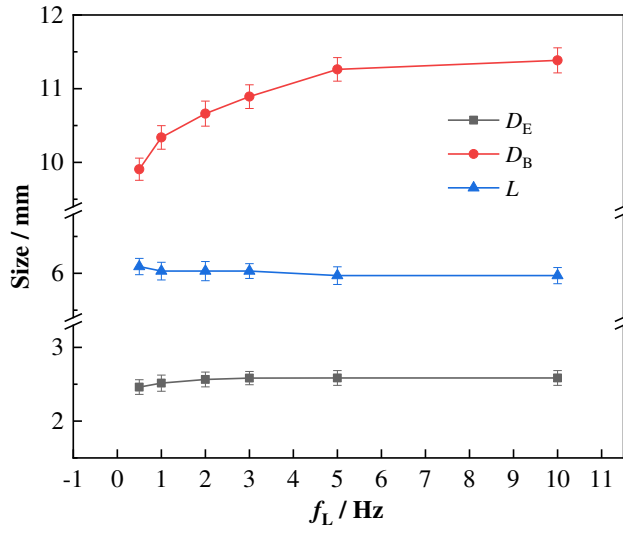
(a) Arc images

(b) Sizes of D_B, D_E and L

Fig.7 Arc images, sizes of D_B, D_E and L in t_P at different f_L

Arc profile in t_b

Fig.8a and Fig.8b illustrate the arc images and their corresponding feature sizes in low-frequency pulse base stage at different f_L, respectively. From the figure, the changing trends of D_B, D_E and L with f_L were all completely opposite to those in t_p, while the variations of D_B, D_E and L were roughly similar. When f_L increased from 0.5 to 3 Hz, D_B and D_E rose from 9.9 mm and 2.4 mm to 10.9 mm and 2.5 mm, respectively. They then gradually stabilized at around 11.3 mm and 2.6 mm as f_L increased to 10 Hz. L was 6.1 mm when f_L was 0.5 Hz. It decreased slightly and fluctuated between 6.0 mm and 5.9 mm as f_L further increased. In t_b, the arc profile expanded, showing that D_B and D_E increased and L decreased, with the increased of f_L.

(a) Arc images

(b) Sizes of D_B, D_E and L

Fig.8 Arc images, sizes of D_B, D_E and L in t_b at different f_L

Arc profile pulsation between t_p and t_b

  The differences of D_B, D_E and L between t_p and t_b (ΔD_B, ΔD_E and ΔL) were defined to represent the pulsation effect of arc profile. ΔD_B, ΔD_E and ΔL at different low-pulsed frequency were calculated and shown in Fig.9. It can be seen that with the increase of f_L, the variation of ΔD_B was most obvious, and the variations of ΔD_E and ΔL were relatively small. ΔD_B and ΔD_E decreased, while ΔL increased with increasing f_L. As f_L changed from 0.5 to 3 Hz, ΔD_B and ΔD_E fell down from 7.1 mm and 0.8 mm to 4.7 mm and 0.4 mm, respectively. They then gradually decreased to 4.0 mm and 0.3 mm, respectively, as f_L increased to 10 Hz. ΔL increased from 0.3 mm to 0.7 mm when f_L varied from 0.5 to 1 Hz. It then fluctuated within a small range, less than 0.1 mm, as f_L further increased. In a word, the pulsation effect of arc profile decreased with increasing f_L. Based on the experimental results, empirical correlations between f_L and ΔD_B, ΔD_E as well as ΔL were respectively established through polynomial fitting, which can be expressed by Equations 6-8.

$$\Delta D_B(f_L) = -0.0132f_L^3 + 0.2624f_L^2 - 1.6681f_L + 7.7051 \quad R^2 = 0.9871 \tag{6}$$

$$\Delta D_E(f_L) = -0.0038f_L^3 + 0.0641f_L^2 - 0.3181f_L + 0.8972 \quad R^2 = 0.9242 \tag{7}$$

10

$$\Delta L(f_L) = 0.0036 f_L{}^3 - 0.0665 f_L{}^2 + 0.3548 f_L + 0.2056 \qquad R^2 = 0.6952 \qquad (8)$$
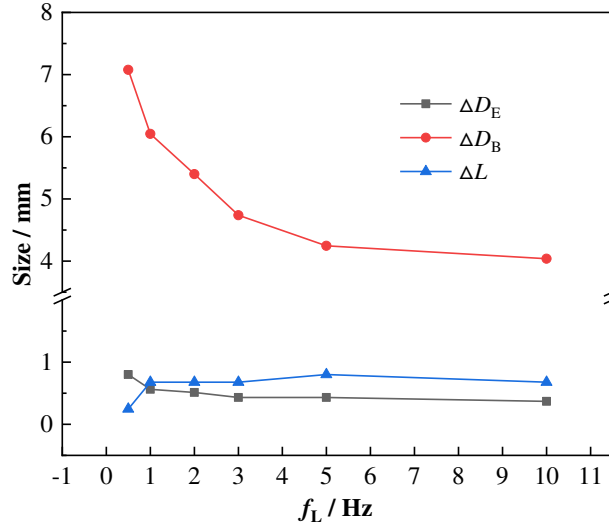

Fig.9 ΔD_B, ΔD_E and ΔL at different f_L

The variation in arc profile with f_L could be interpreted by the difference of light energy in t_p (Q_p) and t_b (Q_b), which is defined as light energy pulsation effect (ΔQ). ΔQ is given by Equation 9.

$$\Delta Q = Q_p - Q_b$$
$$= \eta_{ARC} \cdot \frac{f_v}{f_L} \cdot \left\{ \left[\left(I_{pp} + I_{HP\text{-}avg} \right) U_{pp} + I_{pn} U_{pn} \right] \cdot \delta - \left[\left(I_{bp} + I_{HP\text{-}avg} \right) U_{bp} + I_{bn} U_{bn} \right] \cdot (1 - \delta) \right\} \qquad (9)$$

From the Equation 9, it is found that the light energy pulsation between t_p and t_b is inversely proportional to f_L. Namely ΔQ, which determines the difference in arc profile between t_p and t_b, decreases linearly with the increase of f_L. As the other process parameters remain constant, the arc profile thereby exhibits a shrinking trend in t_p and an expanding trend in t_b. Therefore, the low-frequency pulsation effect of arc profile decreased with increasing f_L.

3.3 Effects of low-pulsed frequency on weld formation

As the heat and force source in the welding process, the welding arc directly acts on the heat and mass transfer process inside the weld pool, and ultimately determines the formation characteristics and quality of the weld bead. During DP-VPTIG welding process, in t_p, the expanded arc with higher heat and force effect induced a wider weld pool width and a higher penetration depth with obvious depressed deformation of the weld pool surface, as shown in Fig.10a. In t_b, the shrunk arc profile with lower heat and force effect led to a narrower weld pool width and a lower penetration depth with the disappearance of the depressed deformation of the weld pool surface, as revealed in Fig.10b. Consequently, under the influence of the periodic variation in arc profile, the pulsation effect of weld formation in both surface appearance and penetration depth was formed. Since the pulsation effect became nearly indistinguishable when f_L was higher than 3 Hz, Tests 1−4 (f_L=0.5−3 Hz) were carried out for the analysis of weld formation characteristics.
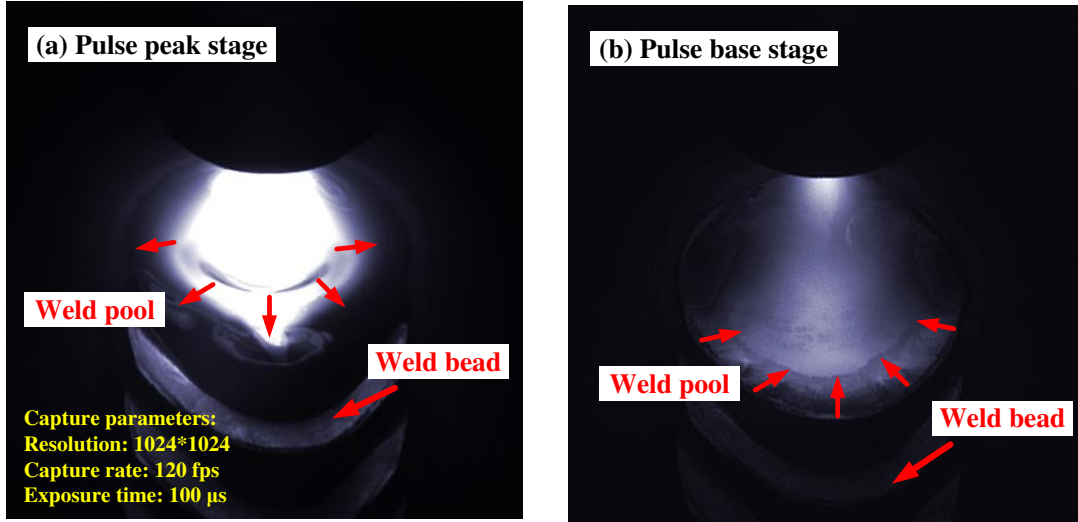
Fig.10 Weld pool morphology in t_p and t_b (f_L=0.5 Hz)
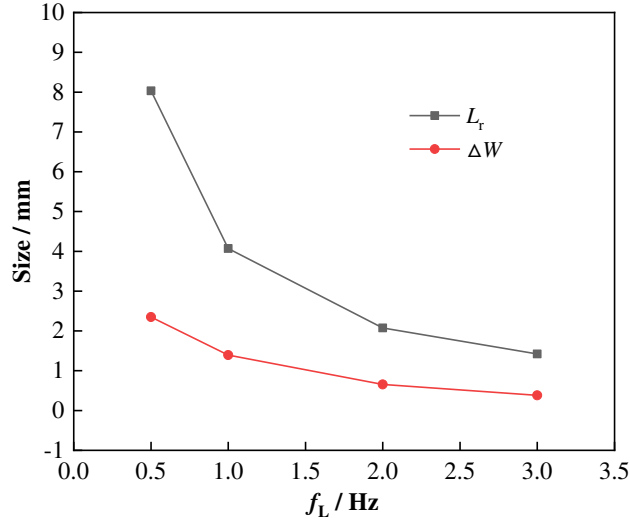
Weld appearance

The weld surface appearances at different f_L are displayed in Fig.11a. The fish-scale ripple shaped weld surface formed due to the pulsation effect of arc profile. As shown in the figure at 0.5 Hz, the weld fish-scale ripple characteristics, namely the pulsation effect of weld appearance, was studied by fish-scale ripple spacing L_r and the difference of fish-scale ripple width ΔW (ΔW=W_p- W_b). Fig.11b illustrates the sizes of L_r and ΔW versus f_L. It can be seen that both ΔW and L_r decreased monotonously with the increase of f_L. When f_L was 0.5 Hz, the size of L_r was 8 mm and ΔW was 2.4 mm (W_p=15.1 mm, W_b=12.7 mm), and obvious fish-scale ripple characteristics could be observed. As f_L increased, ΔW and L_r reduced at a smaller drop rate. The size of L_r was 1.4 mm and ΔW was 0.3 mm (W_p=12.0 mm, W_b=11.7 mm), and the fish-scale ripple characteristics became quite weak when f_L was 3 Hz. According to the experimental results, L_r and ΔW as a function of low-pulsed frequency f_L were empirically correlated, as given by Equations 10 and 11.

$$L_r(f_L) = -1.3133 f_L^{3} + 8.5492 f_L^{2} - 18.449 f_L + 15.284 \quad R^2 = 1 \tag{10}$$

$$\Delta W(f_L) = -0.2204 f_L^{3} + 1.5546 f_L^{2} - 3.8588 f_L + 3.918 \quad R^2 = 1 \tag{11}$$

(a) Weld appearance

12
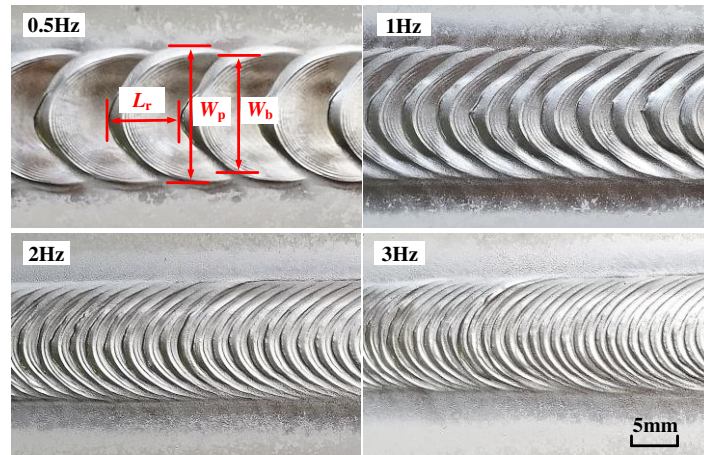
(b) Sizes of L_r and ΔW

**Fig.11 Weld appearance, sizes of L_r and ΔW versus f_L**

Weld penetration

Fig.12a shows the macrograph of weld longitudinal section at different f_L. The weld penetration profile exhibited a fluctuating characteristic with the low-frequency pulse period. In t_p, the penetration D_p was high due to the strong arc heat and force effect, while in t_b the penetration D_b was relatively low caused by the reduction in current amplitude. The pulsation effect of weld penetration was characterised by the difference of penetration ΔD ($\Delta D = D_p - D_b$) between t_p and t_b. The sizes of ΔD, D_p and D_b with different f_L are shown in Fig.12b. With the similar changing trend to those of L_r and ΔW, the size of ΔD decreased monotonously with increasing f_L. ΔD was 0.9 mm ($D_p = 3.4$ mm, $D_b = 2.5$ mm) when f_L was 0.5 Hz, and the fluctuation in weld penetration between t_p and t_b was very significant. As f_L increased to 3 Hz, the size of ΔD reduced to less than 0.2 mm ($D_p = 3.4$ mm, $D_b = 3.2$ mm), meaning that the pulsation effect in weld penetration between t_p and t_b almost disappeared, which was consistent with the pulsation effect of weld appearance and arc profile.

The correlation between ΔD and f_L can be empirically expressed by polynomial fitting Equation 12, based on the experimental results. It can be inferred that the pulsation effect in arc profile, weld appearance and penetration with respect to low-pulsed frequency can be distinctly controlled by following the empirical equations.

$$\Delta D(f_L) = -0.1f_L^3 + 0.6652f_L^2 - 1.5402f_L + 1.513 \quad R^2 = 1 \tag{12}$$

Owing to the low-frequency pulsation effect, in t_p, the high current value could increase the arc penetrating ability to obtain the desired penetration depth, and in t_b the overall heat input could be reduced due to the reduction in current value. It is flexible to balance the arc heat and force effect through adjusting the low-frequency pulse parameters [13]. From the above results, when low-pulsed frequency f_L is less than 0.5 Hz, the arc pulsation effect is so strong that makes the weld formation significantly discontinuous, thereby largely reducing the effective weld width and penetration. When f_L is higher than 3 Hz, the arc pulsation effect almost disappears, which greatly weakens the advantage of low-frequency pulsation effect.

13

Therefore, in order to properly exert the low-frequency pulsation effect, it is recommended to use the low-pulsed frequency of 1–2 Hz in the DP-VPTIG welding of aluminum alloys.
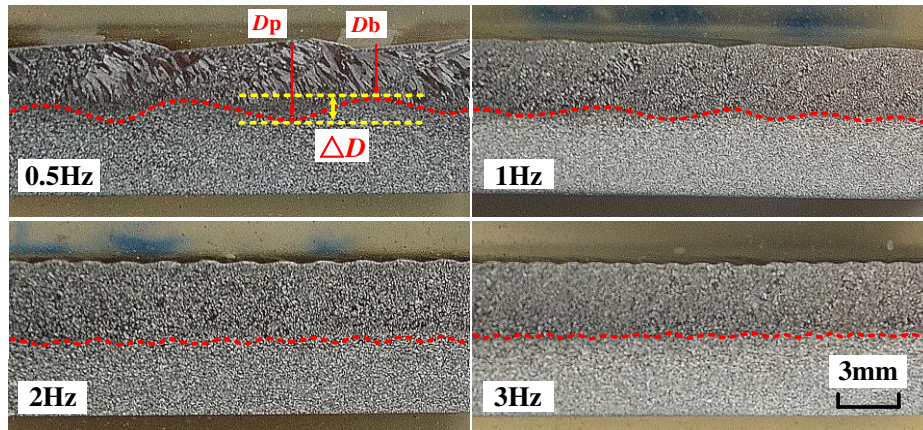
(a) Weld longitudinal section profile
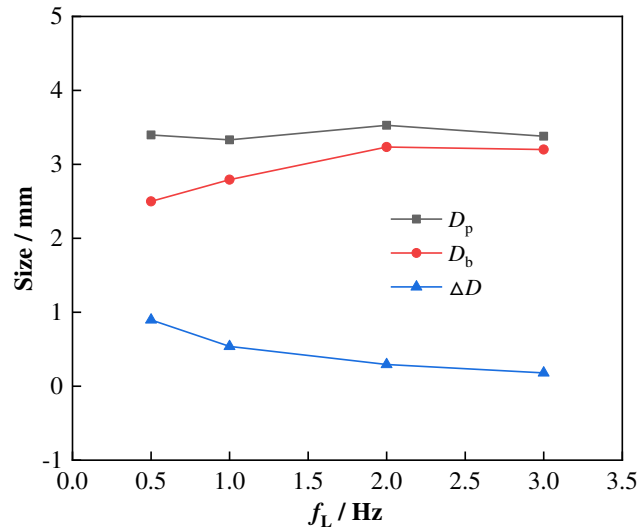
(b) Sizes of D_p, D_b and ΔD

Fig.12 Weld longitudinal section profile, sizes of D_p, D_b and ΔD versus f_L

With the low-frequency pulsation effect of the arc profile, the weld pool fluid could be enhanced and the crystal structure as well as the mechanical properties of the welded joint would thereby be affected. From the macrograph of the weld zone along longitudinal section in Fig.12a, it can be observed that the morphology and distribution of the microstructure varied obviously under different low-pulsed frequencies. The refinement of the grain structure could be found as f_L increased. The microstructure evolution and mechanical properties of the aluminium alloy welded joint produced by DP-VPTIG process need to be further studied.

4 Conclusions

The low-pulsed frequency in double-pulsed VPTIG (DP-VPTIG) welding of AA2219 aluminum alloy and its influence on arc profile, weld appearance and penetration characteristics have been investigated. An image processing algorithm was proposed for arc edge extraction and arc feature sizes acquisition. The main conclusions are drawn as follows:

(1) The arc energy equations in low-frequency pulse peak stage (t_p) and base stage (t_b) were established

based on the electrical parameters. The arc profile periodically expanded in t_p and shrunk in t_b, resulted from the difference in arc energy of the two stages.

(2) The arc profile pulsation effect, defined by the difference of arc profile between t_p and t_b, showed a decreasing trend with the increase of low-pulsed frequency (f_L). In t_p, the arc profile decreased, while in t_b, it increased with the increase of f_L.

(3) The pulsation effects in weld appearance and penetration exhibited a decreasing trend with f_L. They were obvious when f_L was 0.5 Hz, then became weak and tended to disappear as f_L increased above 3 Hz.

(4) The empirical correlations between f_L and the pulsation effects in arc profile, weld appearance and penetration were respectively developed. To properly exert the low-frequency pulsation effect, it is recommended to use the low-pulsed frequency in the range of 1–2 Hz in the DP-VPTIG welding of aluminum alloys.

Conflict of interest

The authors declared that they have no conflicts of interest to this work.

References

[1] Cong BQ, Ding JL, Williams S. Effect of Arc Mode in Cold Metal Transfer Process on Porosity of Additively Manufactured Al-6.3% Cu Alloy. Int J Adv Manuf Technol 2013; 76: 1593–1606.

[2] Lin YT, Wang MC, Zhang Y, He YZ, Wang DP. Investigation of microstructure evolution after post-weld heat treatment and cryogenic fracture toughness of the weld metal of AA2219. Mater Des 2017; 113: 54-59.

[3] Wu H, Chang YL, Mei Q, Liu D. Research advances in high-energy TIG arc welding. Inter J Adv Manuf Technol 2019; 104: 391-410.

[4] Lu SP, Qin MP, Dong WC. Highly efficient TIG welding of Cr13Ni5Mo martensitic stainless steel. J Mater Process Technol 2013; 213: 229-237.

[5] He LB, Li LM, Hao HW, Wu MS, Zhou RL. Grain refinement and high performance of titanium alloy joint using arc-ultrasonic gas tungsten arc welding. Sci Technol Weld Join 2006; 11(1): 72-74.

[6] Niagaj J. Ways to improve the efficiency of welding stainless steel. Weld Int 2014; 28(1) : 45-53.

[7] Kumar TS, Balasubramanian V, Sanavullah MY. Influences of pulsed current tungsten inert gas welding parameters on the tensile properties of AA 6061 aluminum alloy. Mater Des 2007; 28: 2080-2092.

[8] Yang MX, Zheng H, Qi BJ, Yang Z. Effect of arc behavior on Ti-6Al-4V welds during high frequency pulsed arc welding. J Mater Process Technol 2017; 243: 9-15.

[9] Fang YX, Liu ZM, Cui SL, Zhang Y, Qiu JY, Luo Z. Improving Q345 weld microstructure and mechanical properties with high frequency current arc in keyhole mode TIG welding. J Mater Proc Technol 2017; 250 : 280-288.

[10] Yang Z, Qi BJ, Cong BQ, Liu FJ, Yang MX. Microstructure, tensile properties of Ti-6Al-4V by ultra

high pulsefrequency GTAW with low duty cycle. J Mater Proc Technol 2015; 216: 37-47.

[11] Cui SL, Liu ZM, Fang YX, Luo Z, Sunusi MM, Yi S. Keyhole process in K-TIG welding on 4 mm thick 304 stainless steel. J Mater Proc Technol 2017; 243: 217-228.

[12] Wang YP, Qi BJ, Cong BQ, Yang MX, Liu FJ. Arc characteristics in double-pulsed VP-GTAW for aluminum alloy. J Mater Process Technol 2017; 249: 89-95.

[13] Wang YP, Qi BJ, Cong BQ, Yang MX, Zhu MJ, Lin SB. Keyhole welding of AA2219 aluminum alloy with double-pulsed variable polarity gas tungsten arc welding, J Manuf Process 2018; 34: 179-186.

[14] Wang YP, Cong BQ, Qi BJ, Yang MX, Lin SB. Process characteristics and properties of AA2219 aluminum alloy welded by double pulsed VPTIG welding. J Mater Process Technol 2019; 266: 255-263.

[15] Liu A, Tang X, Lu F. Arc profile characteristics of Al alloy in double-pulsed GMAW. Int J Adv Manuf Technol 2013; 65: 1–7.